Mean deformation metrics for quantifying 3D cell–matrix interactions without requiring information about matrix material properties

David A. Stout[a,1], Eyal Bar-Kochba[b,1], Jonathan B. Estrada[b,1], Jennet Toyjanova[b], Haneesh Kesari[b], Jonathan S. Reichner[c,d], and Christian Franck[b,e,2]

[a]Department of Mechanical and Aerospace Engineering, California State University, Long Beach, CA 02903; [b]School of Engineering, Brown University, Providence, RI 02912; [c]Department of Surgery, Rhode Island Hospital, Providence, RI 02903; [d]Department of Surgery, The Warren Alpert Medical School of Brown University, Providence, RI 02903; and [e]Center for Biomedical Engineering, Brown University, Providence, RI 02912

Edited by Daniel A. Hammer, University of Pennsylvania, Philadelphia, PA, and accepted by the Editorial Board January 20, 2016 (received for review June 5, 2015)

Mechanobiology relates cellular processes to mechanical signals, such as determining the effect of variations in matrix stiffness with cell tractions. Cell traction recorded via traction force microscopy (TFM) commonly takes place on materials such as polyacrylamide- and polyethylene glycol-based gels. Such experiments remain limited in physiological relevance because cells natively migrate within complex tissue microenvironments that are spatially heterogeneous and hierarchical. Yet, TFM requires determination of the matrix constitutive law (stress–strain relationship), which is not always readily available. In addition, the currently achievable displacement resolution limits the accuracy of TFM for relatively small cells. To overcome these limitations, and increase the physiological relevance of in vitro experimental design, we present a new approach and a set of associated biomechanical signatures that are based purely on measurements of the matrix's displacements without requiring any knowledge of its constitutive laws. We show that our mean deformation metrics (MDM) approach can provide significant biophysical information without the need to explicitly determine cell tractions. In the process of demonstrating the use of our MDM approach, we succeeded in expanding the capability of our displacement measurement technique such that it can now measure the 3D deformations around relatively small cells (∼10 micrometers), such as neutrophils. Furthermore, we also report previously unseen deformation patterns generated by motile neutrophils in 3D collagen gels.

traction force microscopy | confocal microscopy | large deformations | neutrophil

Mechanical cues within the cellular microenvironment regulate numerous fundamental functions including cell adhesion, deformation, and generation of traction (1–6). Analysis of cellular force generation, and its role in regulating homeostasis across a variety of cellular phenotypes and experimental platforms, has received much attention over the last three decades (7–13). Experimental quantification of cellular forces has produced several cell traction measurement techniques, ranging from surface wrinkle detection and flexure of micropillars to traction force microscopy (TFM) (12, 14–20). In TFM, measured cell-induced displacements are converted into tractions using various mathematical frameworks (14, 15, 17, 18, 21, 22). Both two- and 3D TFM techniques have steadily increased in sophistication and now feature high-spatial displacement resolution and advanced computational formalisms to connect this displacement information to complex material constitutive laws (17, 23, 24).

To successfully perform TFM, it is critical to know the stress–strain constitutive behavior of the matrix surrounding the cell. Although many TFM substrates feature relatively simple artificial gel constructs, such as polyacrylamide and polyethylene glycol, these constructs are impenetrable by cells and obviate measures obtained while cells are in a 3D setting (as would be the case within a bodily tissue). Most physiologically important matrices have complicated, hierarchical microstructures and tend to be spatially heterogeneous. In addition, many cells apply significant forces leading to large matrix deformations that require more complicated, nonlinear constitutive laws for accurate calculation (17, 24–28). Moreover, to generate a quantitative map of tractions exerted by a moving cell, the mechanical properties of the surrounding matrix must be resolved at the cellular level. Taken together, significant experimental challenges exist for accurately deducing the microconstitutive laws for many physiologically realistic matrices and, by extension, the ability to map tractions onto small cells is lacking. Furthermore, and perhaps most importantly, many cells are known to actively remodel the matrix as they move through it. As a result, the constitutive laws are constantly evolving, making a one-time measurement of the matrix material properties insufficient for accurate determination of cell tractions in real time.

To circumvent this fundamental hurdle of requiring a material's constitutive law, we present an alternate, kinematics-based quantification method that correlates cellular deformations to biological function. Based solely on the displacement field in the surrounding matrix, we define tensor-valued mean deformation metrics (MDM) that quantify the overall shape change of the cell

Significance

Investigations in mechanobiology rely on correlation of cellular processes with mechanical signals, such as matrix stiffness and cell tractions. Almost all cell traction and force quantification methodologies require knowledge of the underlying mechanical properties of the extracellular matrix to convert displacement data into corresponding traction data, which restricts the use of these techniques to systems in which the material properties are known. To overcome this hurdle, we present a new approach that does not require any knowledge of the underlying matrix properties but rather makes use of the intrinsically recorded kinematic displacement data. Through rigorous validation and an application to a neutrophil disease model, we show that such an approach produces both accurate and biologically significant information.

Author contributions: D.A.S., E.B.-K., J.B.E., H.K., J.S.R., and C.F. designed research; D.A.S., E.B.-K., J.B.E., J.T., and H.K. performed research; D.A.S., E.B.-K., J.B.E., J.T., H.K., and C.F. contributed new reagents/analytic tools; E.B.-K., J.B.E., J.T., H.K., J.S.R., and C.F. analyzed data; and D.A.S., E.B.-K., J.B.E., H.K., J.S.R., and C.F. wrote the paper.

The authors declare no conflict of interest.

This article is a PNAS Direct Submission. D.A.H. is a guest editor invited by the Editorial Board.

[1]D.A.S., E.B.-K., and J.B.E. contributed equally to this work.

[2]To whom correspondence should be addressed. Email: franck@brown.edu.

This article contains supporting information online at www.pnas.org/lookup/suppl/doi:10.1073/pnas.1510935113/-/DCSupplemental.

(e.g., contractility, mean volume change, and rotation). Because of its kinematic nature, the mean deformation metric approach does not aim to provide any information about the cell tractions. Rather, the approach should be viewed as a distinct, immediately applicable methodology complimentary to TFM for investigations in which the material properties of the extracellular matrix are unknown.

Thus, the mean deformation metric approach provides a significant advantage to laboratories and investigators who may not have the means to conduct sophisticated material characterization measurements at cellular length scales. The method is also well-suited for studies using primary cells for which fluorescent transfection approaches, such as in the use of FRET-based force sensors (29), are not applicable.

We present the formulation of the MDM and validate our technique using well-established analytical solutions, demonstrating our technique is accurate to within 1%. Next, we apply our MDM approach to analyze neutrophil-generated collagen matrix displacement fields obtained using confocal microscopy and fast iterative digital volume correlation (FIDVC) (30). In the process of demonstrating the MDM approach, we solved the challenging problem of resolving local displacements around neutrophils (which are only 10 μm in size) with submicron resolution, and subsequently revealed previously unknown deformation patterns during the migration of neutrophils through a 3D collagen matrix.

MDM

The motion and the deformation of the cell and the surrounding matrix are described using the framework of continuum mechanics as

$$\boldsymbol{x}(\boldsymbol{X},t)=\boldsymbol{u}(\boldsymbol{X},t)+\boldsymbol{X}, \quad [1]$$

where $\boldsymbol{X}$ is the particle's position vector in the cell's initial or reference configuration, $\boldsymbol{x}$ is its position vector at time t, and $\boldsymbol{u}$ is the vector-valued displacement field.

The shape and size changes (strain measures) of infinitesimal material volume, surface, and line elements containing the particle $\boldsymbol{X}$ can be determined using the deformation gradient tensor

$$\mathbf{F}(\boldsymbol{X},t)=\nabla\boldsymbol{x}(\boldsymbol{X},t), \quad [2]$$

where the operator ∇ gives the gradient of a vector-valued function with respect to $\boldsymbol{X}$. Considering the highly heterogeneous and complicated nature of the cell, it is unlikely that $\mathbf{F}$ will be well-defined at each of the cell's material points. Consequently, we define a mean deformation gradient tensor, $\langle\mathbf{F}\rangle$, for the entire cell as

$$\langle\mathbf{F}\rangle:=\frac{1}{\mathrm{vol}(V_0)}\int_{V_0}\mathbf{F}\,dV, \quad [3]$$

where dV is an infinitesimal volume element of the cell in its reference configuration V_0 and $\mathrm{vol}(V_0)$ is the volume of V_0. We believe that $\langle\mathbf{F}\rangle$, which is defined for the entire cell, is more meaningful than $\mathbf{F}$, which is defined pointwise. Mean deformation gradient tensors, defined in a way similar to ours, were used by Hill (31) in the development of theories of effective mechanical behavior of heterogeneous media, such as polycrystals and composites.

The quantity $\langle\mathbf{F}\rangle$ is a very useful metric for understanding the cell's overall deformation. An important advantage of using $\langle\mathbf{F}\rangle$ is that it can be computed solely from the displacements of the cell's surface points. Specifically, it can be shown using the divergence theorem that

$$\langle\mathbf{F}\rangle=\frac{1}{\mathrm{vol}(V_0)}\int_{\partial V_0}\boldsymbol{x}\otimes\boldsymbol{n}\,dA, \quad [4]$$

where ∂V_0 is the boundary of V_0, dA is an infinitesimal element of ∂V_0, $\boldsymbol{n}$ is the unit vector normal to dA, and the symbol $\otimes$ denotes the dyadic product. For computing $\langle\mathbf{F}\rangle$ using Eq. **4**, we approximate the position vectors of the cell's surface points using the position vectors of their nearby matrix points.

Analogous to $\langle\mathbf{F}\rangle$, we define the mean displacement gradient $\langle\nabla\boldsymbol{u}\rangle$ as

$$\langle\nabla\boldsymbol{u}\rangle:=\frac{1}{\mathrm{vol}(V_0)}\int_{V_0}\nabla\boldsymbol{u}\,dV, \quad [5]$$

$$\langle\nabla\boldsymbol{u}\rangle=\frac{1}{\mathrm{vol}(V_0)}\int_{\partial V_0}\boldsymbol{u}\otimes\boldsymbol{n}\,dA. \quad [6]$$

It follows from Eqs. **3** and **5** that the mean deformation and displacement gradients are related as

$$\langle\mathbf{F}\rangle=\mathbf{I}+\langle\nabla\boldsymbol{u}\rangle. \quad [7]$$

Once $\langle\mathbf{F}\rangle$ is determined, standard continuum mechanics calculations provide the mean compressibility, contractility, and rotation of the cell. The determinant of $\langle\mathbf{F}\rangle$, written as $\det\langle\mathbf{F}\rangle=\langle J\rangle$, is a measure of the mean compressibility, or volume change ratio, of the cell. Using the polar decomposition theorem $\langle\mathbf{F}\rangle$ can be written as $\langle\mathbf{F}\rangle=\langle\mathbf{R}\rangle\langle\mathbf{U}\rangle$, where $\langle\mathbf{R}\rangle$ is a proper orthogonal tensor and $\langle\mathbf{U}\rangle$ is a symmetric, positive-definite tensor. The tensors $\langle\mathbf{R}\rangle$ and $\langle\mathbf{U}\rangle$ can be termed the mean rotation and mean right stretch tensor, respectively.

The contractility (stretch or compression) of the cell in these primary directions is given by the eigenvalues of $\langle\mathbf{U}\rangle$, denoted as $\langle\lambda_i\rangle$, $i=1,2,3$. The mean rotation of the cell $\langle\theta\rangle$ is computed as

$$\cos\langle\theta\rangle=\frac{\mathrm{tr}(\langle\mathbf{R}\rangle)-1}{2}, \quad [8]$$

where $\mathrm{tr}(\langle\mathbf{R}\rangle)$ is the trace of the mean rotation tensor $\langle\mathbf{R}\rangle$. The cumulative rotation $\langle\Theta\rangle$ is then defined as the time-integral of mean rotation, or

$$\langle\Theta\rangle=\int_0^t|\langle\theta(\tau)\rangle|d\tau. \quad [9]$$

Results and Discussion

Validation. Validation of the MDM was performed using four canonical mechanics examples of well-known analytical forms (Fig. 1 *A–D*): simple stretch (case A; Fig. 1*A*), axial rotation (case B; Fig. 1*B*), simple shear (case C; Fig. 1*C*), and the Eshelby inclusion solution (case D; Fig. 1*D*). The Eshelby inclusion problem is a convenient analytical comparison with cells embedded in a 3D matrix. The problem considers an infinite, isotropic, linear-elastic extracellular matrix with Poisson's ratio ν and Young's Modulus E. The matrix is initially stress-free, with all displacement and strain values initially at zero. A single spherical cell, or inclusion, in the matrix then undergoes a transformation strain (or eigenstrain) ϵ_T, which is resisted by the matrix outside the region. Because the sphere is embedded in the material, strain ϵ_M and displacement $\boldsymbol{u}$ fields are induced in the matrix. The final strain field in the inclusion is given by the sum of the transformation and matrix strain, ϵ_C (Fig. 1 *E–H*). The strain field ϵ_C inside and on the surface of the inclusion is constant, whereas the displacement is found by taking the dot product of ϵ_C with the position vector $\boldsymbol{x}$. The displacement field outside the inclusion $\boldsymbol{u}$ has a closed-form solution given by (32–34) and is a function only of the inclusion radius (32 voxels), transformation strain ϵ_T, spatial position $\boldsymbol{x}$, and Poisson's ratio (chosen as $\nu=0.2$). For each case, the mean deformation gradient tensor, $\langle\mathbf{F}\rangle$ was calculated from the analytical displacement field and surface normals using Eqs. **6** and **7**. The test surface for the deformation was a sphere, meshed using recursive subdivision

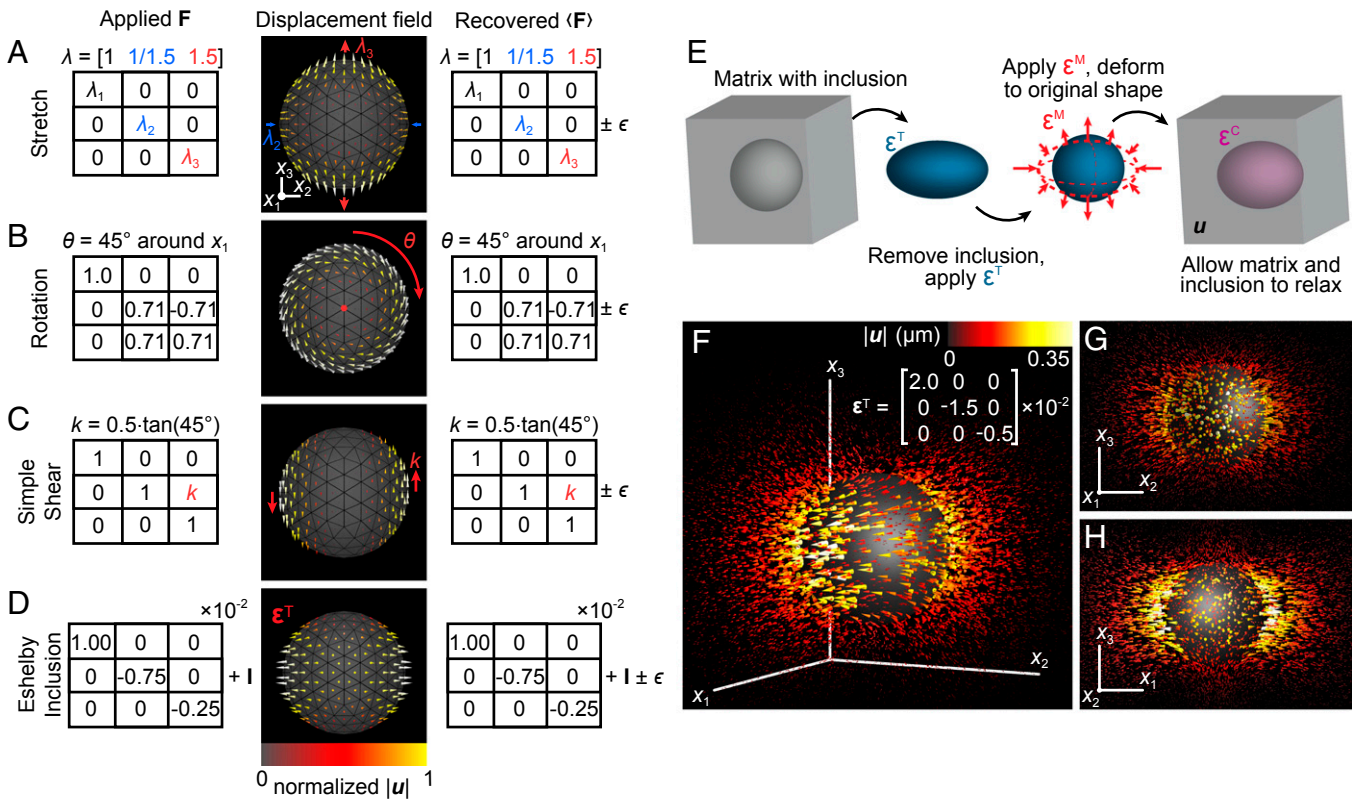

Fig. 1. (*A–D*) Validation of MDM on a spherical cell (gray) undergoing stretch with three stretch ratios λ_1, λ_2, λ_3 (*A*), rotation with angle θ around axis x_1 (*B*), simple shear with magnitude *k* (*C*), and an Eshelby transformation strain ϵ_T (*D*). (*A–D, Left*) Applied deformation gradient **F**. (*A–D, Center*) Vector cone plot of the displacement fields interpolated onto the surface of the sphere for *A–D*, color-coded by normalized magnitude $|\boldsymbol{u}|$. (*A–D, Right*) Results for the recovered mean deformation gradient ⟨**F**⟩ for *A–D* with associated error (ε) (*A–C*, less than 10^{-12} because of numerical error; *D*, less than 10^{-5} because of small strain assumption). Calculation of full-field matrix displacements using the analytical Eshelby solution for an inclusion undergoing an eigenstrain. (*E*) Schematic illustrating the canonical Eshelby inclusion problem, where an initially spherical inclusion (gray) in an infinite matrix undergoes an eigenstrain ϵ_T and induces a known analytical displacement field $\boldsymbol{u}$ and confinement strain ϵ_C external to its boundary. (*F*) Vector cone plot of the solution of the matrix displacements calculated analytically from the inclusion eigenstrain ϵ_T. For visualization purposes, the displacement field is interpolated onto random locations as vector cones color-coded by magnitude $|\boldsymbol{u}|$. (*G* and *H*) $x_2 - x_3$ (*G*) and $x_1 - x_3$ (*H*) plane views of the solution in *F*.

starting from an icosahedron. For cases A to C, the number of subdivisions was two resulting in 320 discrete triangles, and for case D, the number of subdivisions was four, resulting in 5,120 discrete surface triangles. Error from the analytical solution was on the order of 10^{-12} for cases A to C, because of numerical error, and on the order of 10^{-5} for the Eshelby inclusion solution (case D), predominantly because of the assumption of small-strain conditions.

Application of the MDM Approach for the Directional Contractility, Compressibility, and Rotation of Cells. We resolve the spatiotemporal surface features of cell-induced matrix deformations of a small, migrating human neutrophil (<10 μm) in a fibrous 3D collagen matrix. Specifically, we encapsulate primary human neutrophils in a reconstituted type I collagen gel of a final concentration of 2.2 mg/mL, resulting in the fibrillar microstructure shown (Fig. 2*A* and Fig. S1 *A* and *B*). The collagen fibers are visualized in blue via confocal reflectance microscopy, and the neutrophil is visualized via the membrane stain 1,1′-Dioctadecyl-3,3,3′,3′-Tetramethylindocarbocyanine Perchlorate (DiI; Life Technologies) in red. Simultaneous injection of 0.5-μm carboxylate-modified green fluorescent spherical particles (Fig. 2*A*, *Right*) during collagen polymerization serves as means for tracking the 3D matrix deformations imparted by the locomoting cell. To determine the cell-induced 3D displacement field, we use our previously developed FIDVC algorithm (30). This algorithm converts the motion of fiduciary markers obtained from time-lapse confocal image volumes into a 3D displacement field of matrix deformations around the neutrophil (Fig. 2*B*). Full-field displacement can then be mapped to the rendered cell surface via interpolation (Fig. 2*C*). Our FIDVC algorithm accurately measures large material deformations, which we find significant during neutrophil locomotion in collagen because the local displacement gradient, $\nabla\boldsymbol{u}$, is nonnegligible (Fig. S2 *A–G*). The FIDVC algorithm spatially refines the correlation windows, therefore allowing the capture of significantly higher spatial resolutions while increasing signal-to-noise and computational efficiency compared with our previous digital volume correlation (DVC) method (35). The displacement sensitivity in our study was 0.04, 0.06, and 0.18 μm (x_1, x_2, and x_3, respectively), with a chosen spatial grid resolution set to eight voxels (~1.7 for x_1 and x_2 and 2.4 μm for x_3). The typical computation time on a graphics processing unit-equipped personal computer to determine the 3D cellular deformation field between two successive 512 × 512 × 128 voxel volumes is approximately 1–2 min. Whereas the FIDVC natively provides a detailed full-field map of the entire matrix displacements in the vicinity of the cell, many practical applications require simpler biomechanical classification metrics. In traditional TFM studies, these metrics include simple scalar quantities such as root-mean-squared tractions, total forces, strain energies, and contractility measures such as the trace of the dipole tensor (7, 15, 18, 36). However, computation of these metrics requires the constitutive behavior of the matrix. The MDM approach, on the other hand, can provide biomechanical metrics without the use of the matrix constitutive law or having to solve a large system of equations.

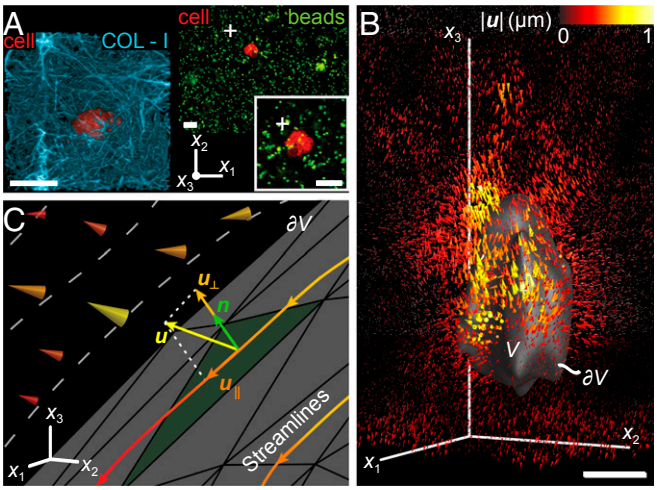

Fig. 2. Cell-induced hydrogel deformations and calculation of surface displacements. (*A*, *Left*) Volume rendering of a Dil-stained neutrophil (red) embedded in a fibrillar type I collagen matrix (cyan) imaged with reflectance confocal microscopy. (*A*, *Right*) Confocal micrograph of a neutrophil (red) migrating in a 3D collagen matrix containing randomly distributed 0.5-μm fluorescent microspheres (green) used to measure cell-induced displacement fields. (Scale bar, 10 μm.) (*B*) Vector cone plot of the induced 3D displacement field measured by FIDVC surrounding a chemotactic neutrophil (gray) with volume V and surface ∂V. (Scale bar, 5 μm.) (*C*) Schematic outlining the interpolation of the 3D displacement field to ∂V to produce the surface displacements $\boldsymbol{u}$. The surface normal $\boldsymbol{n}$ (green) is used to calculate the corresponding normal $\boldsymbol{u}_\perp$ and tangential $\boldsymbol{u}_\parallel$ component of $\boldsymbol{u}$ with respect to the cell.

All of the biomechanical metrics in the MDM approach are defined solely using the displacement data from the cell–matrix boundary and the geometry of the cell–matrix boundary, which allows the approach to maintain an inherently low measurement noise floor that is significantly smaller than current state-of-the-art cell–matrix quantification methodologies (15, 17, 18, 37).

We determined $\langle \mathbf{F} \rangle$ from Eq. **7** for naïve (N) and lipopolysaccharide (LPS)-treated (L) neutrophils undergoing either chemokinesis (K) or chemotaxis (T). The mean compressibility $\langle J \rangle$ for the different phenotypes is shown in Fig. 3*A*. Principal directions in which the cell stretches/contracts are given by the eigenvectors $\langle \boldsymbol{N}_i \rangle$ of $\langle \mathbf{U} \rangle$, whereas cell contractility in these directions is given by the eigenvalues of $\langle \mathbf{U} \rangle$, $\langle \lambda_i \rangle$, where $i = 1, 2, 3$. The mean contractilities $\langle \lambda_i \rangle$ are plotted for the different neutrophil phenotypes in Fig. 3*B*. Examination of the contractility in conjunction with the cell compressibility reveals that neutrophils behave isochorically, contracting along two of the principal directions $\langle \boldsymbol{N}_1 \rangle$ and $\langle \boldsymbol{N}_2 \rangle$ while extending along the third axis $\langle \boldsymbol{N}_3 \rangle$ (Fig. 3*B* and Fig. S2*I*). Such behavior is indicative of a contractile, integrin-dependent mode of motility as opposed to a pushing, or integrin-independent mechanism (38). These observations are consistent with recent findings showing that integrins continue to play a significant regulatory role for traction generation and motility under confinement in the presence of ligands (39). Using the simple MDM, we detect statistically significant differences between naïve and LPS-activated human neutrophils. LPS-activated neutrophils demonstrate a significant increase in overall contractility (Fig. 3*B* and Fig. S2*G*) and a trend toward a greater capacity to undergo changes in volume (Fig. 3*A*).

The mean rotation $\langle \theta \rangle$ of the different types of cells is shown in Fig. 3 *E* and *F*. The figure shows, for the first time to our knowledge, that neutrophils in the presence of LPS undergo significant rotatory motion, as quantified by a marked increase in the average rotation angle (Fig. 3*E*) and cumulative rotation (Fig. 3*F*). We find statistically significant increases across all evaluated biomechanical metrics (Fig. 3 *A*–*F*) for both chemokinesis (K) and chemotaxis (T).

The capability to deduce cell mean compressibility, directional cell contractility, and cell rotations from displacement information is an important feature of the MDM approach. The information contained in these mean metrics is challenging to capture by current TFM methodologies or 3D image reconstruction algorithms.

Resolving Local Displacements Around Neutrophils with Submicron Resolution Using FIDVC. Full-field vector maps of displacement fields obtained from FIDVC calculations during neutrophil migration through collagen show complex distributions (Fig. 2*B* and Movie S1). Areas of large displacement (yellow) occur in close proximity to the cell surface ∂V (gray) and quickly decay in the far-field. To clearly interpret surface localization of the displacement field, we interpolate $\boldsymbol{u}$ onto a discretized triangular mesh structure of the cell surface with normal, $\boldsymbol{n}$ (Fig. 4*A*), and decouple the surface normal $\boldsymbol{u}_\perp$ and tangential $\boldsymbol{u}_\parallel$ components (Fig. 4 *C* and *D*). Tangential displacements are represented with streamlines to assist in visualizing deformation patterns. The canonical inclusion problem by Eshelby (33) was used as quantitative validation of the full-field displacement interpolation procedure, matching the analytical solution to within 10^{-3} percent error (Fig. 1 and Fig. S3).

The surface displacement field (Fig. 4*A*) varies spatially across the entire surface of the cell and is visually viewpoint-dependent,

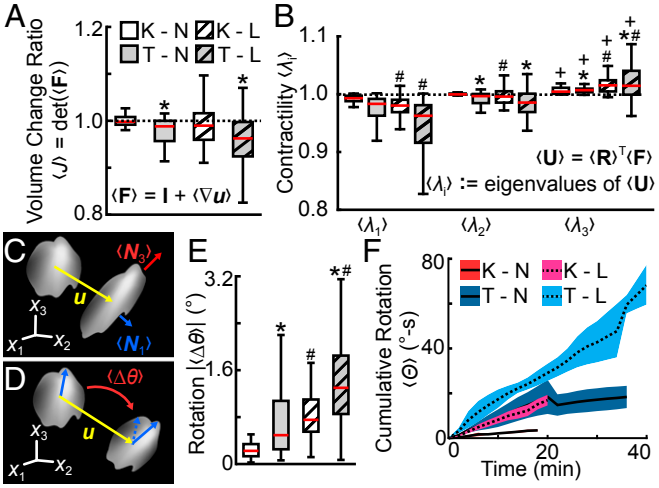

Fig. 3. MDM for neutrophils calculated from the mean deformation gradient tensor $\langle \mathbf{F} \rangle$. (*A*) Boxplot of the mean volume change ratio $\langle J \rangle$ of the cell (dotted line, constant volume), defined as the determinant of $\langle \mathbf{F} \rangle$ for all time points of the tested conditions: K – N, chemokinesis and naïve (solid white; $n = 30$); T – N, chemotaxis and naïve (solid gray; $n = 48$); K – L, chemokinesis and LPS-activated (hatched white; $n = 44$); and T – L, chemotaxis and LPS-activated (hatched gray; $n = 57$). Red lines indicate medians; upper and lower boxes indicate upper and lower quartiles; whiskers indicate maximum and minimum values. (*B*) Boxplot of the three mean contractility values $\langle \lambda_i \rangle$ calculated from the right Cauchy–Green stretch tensor $\langle \mathbf{U} \rangle$. Values of $\langle \lambda_i \rangle$ below 1 signify mean contraction, whereas values of $\langle \lambda_i \rangle$ above 1 are mean expansion of the cell along the associated principal axis. (*C*) Schematic illustrating minimum $\langle \lambda_1 \rangle$ and maximum $\langle \lambda_3 \rangle$ principal stretches exerted by the cell with corresponding eigenvectors $\langle \boldsymbol{N}_1 \rangle$ and $\langle \boldsymbol{N}_3 \rangle$. (*D* and *E*) Schematic illustrating mean cell rotation angle $\langle \theta \rangle$ (*D*) and corresponding boxplot for all time points and conditions (*E*). (*F*) Integrated $\langle \theta \rangle$ for each cell over its migration time t for all tested conditions: K – N (solid red; $n = 4$ cells); T – N (solid blue; $n = 3$ cells); K – L (dashed magenta; $n = 5$ cells); and T – L (dashed cyan; $n = 3$ cells). The middle line indicates the mean; the shaded area indicates the SD of integrals evaluated at the specified time point. $P < 0.05$ by Mann–Whitney U test across corresponding chemokinesis and chemotaxis groups (*), naïve and LPS-activated groups (#), and across $\langle \lambda_i \rangle$ (+) in *B*.

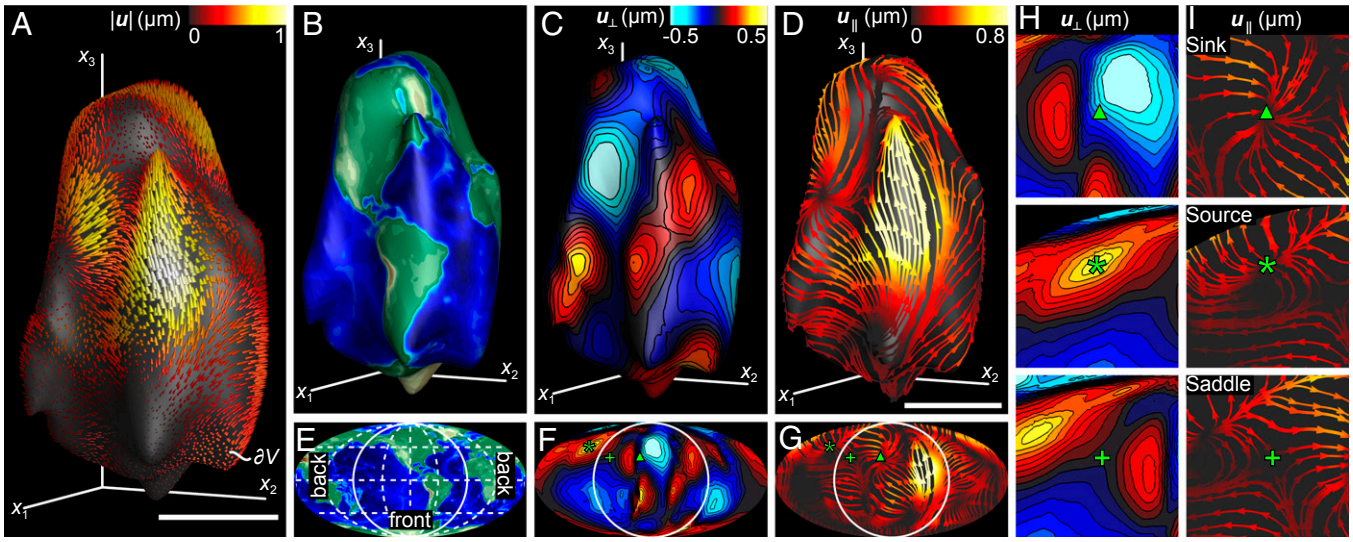

Fig. 4. Measurement of 3D surface displacements exerted by a chemotactic neutrophil and its associated homolographic 2D projections. (*A*) Vector cone plot of the 3D displacement field interpolated onto the surface ∂V (gray) of the neutrophil, color-coded by magnitude $|\boldsymbol{u}|$. (*B*) Elevation data of the Earth projected onto ∂V to illustrate the spatial position of surface data. (*C*) Contour plot of the normal component of $\boldsymbol{u}$ ($\boldsymbol{u}_\perp$) with respect to ∂V, color-coded by direction and magnitude (red is outward and blue is inward normal surface displacement). (*D*) Streamline plot of the tangential displacement component $\boldsymbol{u}_\parallel$ along ∂V, color-coded by magnitude with arrowheads pointing along the vector field. (Scale bar, 5 μm.) (*E*) Mollweide mapping of the spherical projection of Earth's elevation data in *B* to allow for user-friendly visualization of all 3D data onto a plane. Dashed grid lines represent spacing of 45° along latitude and longitude lines. Data interior to the solid white circle are located on the front hemisphere (x_1 > cell centroid on ∂V), whereas data outside lie on the back hemisphere (x_1 < cell centroid on ∂V) of the cell. (*F* and *G*) Mapped contour plot of $\boldsymbol{u}_\perp$ in *C* and streamline plot of $\boldsymbol{u}_\parallel$ in *D* using the Mollweide projection in *E*. (*H* and *I*) Magnified view of *F* and *G* highlighting sink-like (green triangle) (*Top*), source-like (green star) (*Middle*), and saddle-like (green plus symbol) (*Bottom*) features of $\boldsymbol{u}_\parallel$ and $\boldsymbol{u}_\perp$.

complicating feature analysis for the viewer. To address this issue, we use the homolographic Mollweide mapping technique to cast 3D surface data into viewpoint-independent 2D contour plots (Fig. 4 *E*–*G*). For illustration, the Earth's topological data (Fig. 4*B*) is mapped from a spherical projection of the neutrophil surface into a familiar 2D globe map (Fig. 4*E*). We apply the same Mollweide mapping to the decoupled surface normal and tangential displacements (Fig. 4 *C* and *D* and Movie S2) on the neutrophil surface to visualize the complex local out-of-plane and in-plane deformations in convenient 2D contour maps (Fig. 4 *F* and *G*). Detailed examination of specific regions along the cell surface reveal previously undocumented deformation structures reminiscent of sink, source, and saddle point flow structures (Fig. 4 *H* and *I*) commonly found in moving fluids. To our knowledge, these are the first observations of such well-defined deformation structures within the cell-generated displacement fields of a moving leukocyte.

Conclusion

We present a new approach for quantifying cell–matrix interactions in mechanically complex microenvironments, such as 3D collagen gels, based purely on kinematic measurements. Similar to traditional TFM, we establish a set of new mean kinematic metrics to describe significant phenotypical differences between naïve and LPS-activated human neutrophils. Because our technique does not require any knowledge of the mechanical properties of the surrounding matrix, it can be applied to virtually any complex tissue including fibrous networks, multilayer scaffolds, and any transparent living tissue. Applications include investigations in which cells actively remodel the matrix during the time window of observation.

The main limitation of the MDM approach, owing to its kinematic nature, is the inability to discern matrix stiffness effects which can only be calculated when the mechanical properties of the matrix are known. In cases where the mechanical properties are known, the FIDVC-derived displacement data can either be quantified using the presented MDM approach or be directly converted to traction data using, for example, our 3D viscoelastic TFM algorithm (see the MDM–TFM comparison chart; Fig. S5) (24).

In parallel to the MDM approach, we resolved spatially varying deformation features across cells about one order of magnitude smaller than what had been shown possible previously. By using 3D surface and cartographic projection methods, we were able to reveal previously unknown 3D cell–matrix displacement patterns, such as source- and sink-type patterns. It is known that any continuous field defined on a 2-sphere will show features that are similar to the source and sink patterns that we observed on the neutrophil cell surfaces. However, we believe that the number of source and sink patterns and their relative spatial arrangement could contain biologically significant information, such as information about the cell's motility and adhesion mechanisms.

Materials and Methods

Three-Dimensional Collagen Gel Preparation for Neutrophil Chemotaxis. Neutrophils were isolated from healthy human volunteers using previously established protocols (39). Institutional review board approval was obtained from the Rhode Island Hospital's Committee on Protection of Human Subjects to allow donation of venous blood. Informed consent was obtained in accordance with the Declaration of Helsinki. Neutrophil chemotaxis was induced via a custom-built three-well planar chemokine diffusion system (Fig. S1); 3D collagen (type I, rat tail; BD Biosciences) matrices were prepared at a 2.2 mg/mL concentration with the addition of 6% (wt/vol) of 0.5-μm yellow-green carboxylate-modified microspheres (Life Technologies). Vybrant Dil-stained (Life Technologies) cells were suspended in Leibovitz's L-15 (phenol-free; Life Technologies) medium with 2 mg/mL glucose added for a final concentration of 10^6 cells/mL and then added to the collagen matrix solution.

Chemotaxis, Chemokinesis, and LPS Activation. For naïve neutrophil chemotaxis experiments, both wells contained Leibovitz's L-15 with 2 mg/mL glucose. The left well also contained 100 μL of the chemoattractant, Formyl-Met-Leu-Phe (fMLF) (Sigma-Aldrich), for a final concentration of 1 μM (Fig. S1*A*). LPS activation was initiated through the addition of 100 ng/mL ultrapure LPS (LPS-EB; InvivoGen). Live-cell imaging took place 5 min after the introduction of either

chemokine or chemokine plus activation solution for each respective experiment. Chemokinesis experiments were performed by adding 1 μM fMLF to both wells in addition to adding 1 μM fMLF into the collagen mixture recipe before polymerization to establish a uniform chemokine concentration profile across the sample before imaging.

Microscopy and Live-Cell Imaging. Three-dimensional image stacks were acquired using a Nikon A-1 confocal system mounted on a Ti-Eclipse inverted optical microscope controlled by NIS-Elements Nikon Software. A Plan Fluor 40× air objective (NA = 0.6; Nikon) mounted on a piezo objective positioner was used for all cell experiments, which allowed imaging speeds of 30 frames per second using a resonant scanner. Yellow-green fluorescent microspheres (0.5 μm; Life Technologies) were dispersed throughout the collagen matrix and excited with an Argon (488 nm) laser. DiI-stained cells were excited with a red HeNe diode (561 nm) laser. Confocal image stacks of 512 × 512 × 128 voxels (108 × 108 × 38 μm^3) were recorded every 2–3 min with a *z*-step of 0.30 μm. To ensure physiological imaging conditions within the imaging chamber, temperature was controlled at 37 °C as previously described (17, 39). For reflectance microscopy, an APO 40× water immersion objective (NA = 1.15; Nikon) with *z*-step = 0.25 μm was used to obtain typical imaging volumes of 167 × 167 × 81 voxels (52 × 52 × 20 μm^3).

Measurement of Cell-Induced Displacements. Cell-induced full-field displacements were measured using the method described by Toyjanova et al. (17); 3D time-lapse images of fluorescent beads embedded in the collagen matrix were captured using laser-scanning confocal microscopy (LSCM). The incremental motion, or displacements, of the fluorescent beads was tracked between time points using our previously developed FIDVC algorithm (30).

Calculating Discretized Cell Surfaces. The 3D cellular surface boundary was determined from volumetric images of the fluorescently labeled cell membrane. A median filter with a 5 × 5 × 5 window was applied to the raw volumetric image to reduce noise. Following a contrast adjustment where 1% of intensity values get saturated, a binary image was generated by setting all intensity values less than 50% of the maximum intensity of the image to 0 (black) and all others to 1 (white). The final binary mask of the cell was generated by removing all but the largest connected component. The triangular surface mesh of the binary mask was computed using the marching cubes algorithm (40) and then smoothed using the algorithm developed by Taubin (41).

ACKNOWLEDGMENTS. The authors acknowledge Xian O'Brien, Angel Byrd, and Mohak Patel for helpful discussions. J.S.R. acknowledges support from NIH Grant GM066194. C.F. and J.S.R. acknowledge support from NIH Grant AI101469 and a Brown University seed grant. D.A.S. acknowledges support from a National Science Foundation Graduate Research Fellowship. J.B.E. acknowledges support from a Graduate Assistance in Areas of National Need (GAANN) fellowship from the Brown University Institute for Molecular and Nanoscale Innovation.

1. Das T, et al. (2015) A molecular mechanotransduction pathway regulates collective migration of epithelial cells. *Nat Cell Biol* 17(3):276–287.
2. Discher DE, Janmey P, Wang YL (2005) Tissue cells feel and respond to the stiffness of their substrate. *Science* 310(5751):1139–1143.
3. Chen CS (2008) Mechanotransduction - a field pulling together? *J Cell Sci* 121(Pt 20): 3285–3292.
4. Levental I, Georges PC, Janmey PA (2007) Soft biological materials and their impact on cell function. *Soft Matter* 3:299–306.
5. Schwarz US, Gardel ML (2012) United we stand: Integrating the actin cytoskeleton and cell-matrix adhesions in cellular mechanotransduction. *J Cell Sci* 125(Pt 13): 3051–3060.
6. Siechen S, Yang S, Chiba A, Saif T (2009) Mechanical tension contributes to clustering of neurotransmitter vesicles at presynaptic terminals. *Proc Natl Acad Sci USA* 106(31): 12611–12616.
7. López-Fagundo C, Bar-Kochba E, Livi LL, Hoffman-Kim D, Franck C (2014) Three-dimensional traction forces of Schwann cells on compliant substrates. *J R Soc Interface* 11(97):20140247.
8. Paszek MJ, et al. (2005) Tensional homeostasis and the malignant phenotype. *Cancer Cell* 8(3):241–254.
9. Paszek MJ, Weaver VM (2004) The tension mounts: Mechanics meets morphogenesis and malignancy. *J Mammary Gland Biol Neoplasia* 9(4):325–342.
10. Aratyn-Schaus Y, Gardel ML (2008) Biophysics. Clutch dynamics. *Science* 322(5908): 1646–1647.
11. Aratyn-Schaus Y, Gardel ML (2010) Transient frictional slip between integrin and the ECM in focal adhesions under myosin II tension. *Curr Biol* 20(13):1145–1153.
12. Sniadecki NJ, et al. (2007) Magnetic microposts as an approach to apply forces to living cells. *Proc Natl Acad Sci USA* 104(37):14553–14558.
13. Ricart BG, Yang MT, Hunter CA, Chen CS, Hammer DA (2011) Measuring traction forces of motile dendritic cells on micropost arrays. *Biophys J* 101(11):2620–2628.
14. Tan JL, et al. (2003) Cells lying on a bed of microneedles: An approach to isolate mechanical force. *Proc Natl Acad Sci USA* 100(4):1484–1489.
15. Butler JP, Tolić-Nørrelykke IM, Fabry B, Fredberg JJ (2002) Traction fields, moments, and strain energy that cells exert on their surroundings. *Am J Physiol Cell Physiol* 282(3):C595–C605.
16. Maruthamuthu V, Sabass B, Schwarz US, Gardel ML (2011) Cell-ECM traction force modulates endogenous tension at cell-cell contacts. *Proc Natl Acad Sci USA* 108(12): 4708–4713.
17. Toyjanova J, et al. (2014) High resolution, large deformation 3D traction force microscopy. *PLoS One* 9(4):e90976.
18. Legant WR, et al. (2010) Measurement of mechanical tractions exerted by cells in three-dimensional matrices. *Nat Methods* 7(12):969–971.
19. Harris AK, Wild P, Stopak D (1980) Silicone rubber substrata: A new wrinkle in the study of cell locomotion. *Science* 208(4440):177–179.
20. Jannat RA, Dembo M, Hammer DA (2011) Traction forces of neutrophils migrating on compliant substrates. *Biophys J* 101(3):575–584.
21. Dembo M, Wang YL (1999) Stresses at the cell-to-substrate interface during locomotion of fibroblasts. *Biophys J* 76(4):2307–2316.
22. del Álamo JC, et al. (2013) Three-dimensional quantification of cellular traction forces and mechanosensing of thin substrata by fourier traction force microscopy. *PLoS One* 8(9):e69850.
23. Sabass B, Gardel ML, Waterman CM, Schwarz US (2008) High resolution traction force microscopy based on experimental and computational advances. *Biophys J* 94(1): 207–220.
24. Toyjanova J, et al. (2014) 3D Viscoelastic traction force microscopy. *Soft Matter* 10(40): 8095–8106.
25. Wang H, Abhilash AS, Chen CS, Wells RG, Shenoy VB (2014) Long-range force transmission in fibrous matrices enabled by tension-driven alignment of fibers. *Biophys J* 107(11):2592–2603.
26. Jansen KA, Bacabac RG, Piechocka IK, Koenderink GH (2013) Cells actively stiffen fibrin networks by generating contractile stress. *Biophys J* 105(10):2240–2251.
27. Wen Q, Janmey PA (2013) Effects of non-linearity on cell-ECM interactions. *Exp Cell Res* 319(16):2481–2489.
28. Vader D, Kabla A, Weitz D, Mahadevan L (2009) Strain-induced alignment in collagen gels. *PLoS One* 4(6):e5902.
29. Borghi N, et al. (2012) E-cadherin is under constitutive actomyosin-generated tension that is increased at cell-cell contacts upon externally applied stretch. *Proc Natl Acad Sci USA* 109(31):12568–12573.
30. Bar-Kochba E, Toyjanova J, Andrews E, Kim K-S, Franck C (2015) A fast iterative digital volume correlation algorithm for large deformations. *Exp Mech* 55(1):261–274.
31. Hill R (1972) On constitutive macro-variables for heterogeneous solids at finite strain. *Proc Roy Soc Lond A Mat* 326:131–147.
32. Eshelby JD (1957) The determination of the elastic field of an ellipsoidal inclusion, and related problems. *Proc Roy Soc Lond A Mat* 241(1226):376–396.
33. Eshelby JD (1959) The elastic field outside an ellipsoidal inclusion. *Proc Roy Soc Lond A Mat* 252(1271):561–569.
34. Bower AF (2011) *Applied Mechanics of Solids* (CRC Press, Boca Raton, FL).
35. Franck C, Hong S, Maskarinec SA, Tirrell DA, Ravichandran G (2007) Three-dimensional full-field measurements of large deformations in soft materials using confocal microscopy and digital volume correlation. *Exp Mech* 47(3):427–438.
36. Tanimoto H, Sano M (2014) A simple force-motion relation for migrating cells revealed by multipole analysis of traction stress. *Biophys J* 106(1):16–25.
37. Del Alamo JC, et al. (2007) Spatio-temporal analysis of eukaryotic cell motility by improved force cytometry. *Proc Natl Acad Sci USA* 104(33):13343–13348.
38. Renkawitz J, Sixt M (2010) Mechanisms of force generation and force transmission during interstitial leukocyte migration. *EMBO Rep* 11(10):744–750.
39. Toyjanova J, Flores-Cortez E, Reichner JS, Franck C (2015) Matrix confinement plays a pivotal role in regulating neutrophil-generated tractions, speed, and integrin utilization. *J Biol Chem* 290(6):3752–3763.
40. Lorensen WE, Cline HE (1987) Marching cubes: A high resolution 3D surface construction algorithm. *Comput Graph (ACM)* 21(4):163–169.
41. Taubin G (1995) A signal processing approach to fair surface design. *Proceedings of the 22nd Annual Conference on Computer Graphics and Interactive Techniques* (Association for Computing Machinery, New York), pp 351–358.
42. Farid H, Simoncelli EP (2004) Differentiation of discrete multidimensional signals. *IEEE Trans Image Process* 13(4):496–508.
43. Gao Y, Kilfoil ML (2009) Accurate detection and complete tracking of large populations of features in three dimensions. *Opt Express* 17(6):4685–4704.